Journal of Asian Concrete Federation

journal homepage: https://jacf.sfulib3.publicknowledgeproject.org/index.php/jacf

Crack Resistance for Rockfill Dam Concrete Face Slabs Based on through Experimental Investigation and Entropy Weight Method

Zhenyang Sun[a], Qiaoling Min[a,b,*], Guosheng Zhang[a,c], Mingchao Li[a,d] , Ajit K Sarmah[e]

[a] *State Key Laboratory of Hydraulic Engineering Intelligent Construction and Operation, Tianjin University, Tianjin 300350, China*
[b] *School of Marine Science and Technology, Tianjin University, Tianjin 300072, China*
[c] *Huanghe Hydropower Development Co., Ltd., Qinghai 810008, China*
[d] *School of Water Resources and Hydropower Engineering, Xinjiang University of Technology, Xinjiang 848023, China*
[e] *Department of Civil and Environmental Engineering, The Faculty of Engineering and Design, The University of Auckland, Private Bag 92019, Auckland 1142, New Zealand*

A B S T R A C T

The harsh climatic conditions in alpine regions often pose challenges to the construction of concrete face rockfill dams. The purpose of this study is to investigate the enhancement of crack resistance in hydraulic concrete for face slabs by systematically comparing internal admixtures including nano-calcium carbonate (NCC), silica fume (SF), silica fume-fly ash composite (SF-FA), magnesium oxide (MgO), and anti-seepage crack-resistant material (ACM). A two-phase experimental approach was adopted: Phase I optimized a reference mix (water-to-binder ratio of 0.35-0.36, fly ash content of 20-30%) for the target project, while Phase II systematically evaluated the workability, mechanical properties, deformation, and durability of the modified concrete. Experimental findings show that SF significantly enhanced mechanical strength, increasing the 28-day compressive strength to 50.1 MPa, while NCC and ACM effectively reduced the 90-day drying shrinkage strain to approximately 300×10^{-6}, compared to 380×10^{-6} for the reference mix. To address inconsistencies in traditional single-index evaluations, an intelligent assessment framework based on the Entropy Weight Method (EWM) was developed, integrating multi-dimensional performance data into a Comprehensive Crack Resistance Index (CCRI). The EWM-based analysis ranked SF, NCC, SF-FA, and MgO as the top four performers based on CCRI. However, considering fresh concrete workability constraints, NCC-concrete, with a slump of 70 mm and the highest overall stability, was identified as the optimal material solution. This data-driven approach provides a validated strategy for enhancing the crack resistance and long-term durability of CFRD face slabs in dry, windy alpine environments.

Keywords: Rockfill dam; Concrete face slab; Admixtures; Entropy Weight Method; Crack resistance index.

1. Introduction

Concrete face rockfill dams (CFRD) utilize earth and rock materials excavated from the dam site for embankment construction, achieving efficient use of rockfill materials based on the earth-rock balance theory. Given their low cost, relative construction simplicity, and strong adaptability to topography and geology, CFRDs have become the preferred dam type in many engineering projects[1-5]. The concrete face slab serves as the most critical impervious structure in a rockfill dam[6]. Thus, crack prevention in the face slab is essential for the rapid construction of CFRDs. However, significant deficiencies in crack prevention persist in the current practice. For instance, during multiple inspections of the Tianshengqiao-I rockfill dam between 1997 and 2000, nearly 6,000 bending stress-induced cracks were identified in the concrete face slabs, with a maximum crack width of 4 mm and a maximum crack depth of 34 cm[7]. In southwestern China, the 156-m high Zipingpu CFRD, suffered a strong earthquake with a Richter magnitude scale of 8.0. The extrusion and uplift failures of various degrees along the upper horizontal construction joints and crushing damage near the middle vertical joints in the concrete slabs occurred[8]. Many cracks also occurred during the construction and operating period of the Shuibuya Dam, the highest CFRD in the world (233 m height). The cracks mainly occurred in the lower and middle parts of the face slab, and most of them were horizontal. Shrinkage stress, temperature-induced stress and the settlement of the foundation of the dam are the main

* Corresponding author: Qiaoling Min (mql2012@tju.edu.cn)

DOI http://dx.doi.org/10.18702/acf.2026.12.2.8

Received: 15-Jan-2026; Revised: 21-Feb-2026; Accepted: 02-Mar-2026; Published online: 27-April-2026

ISSN 2465-7964/eISSN 2465-7972

reasons for the development of the cracks[9].The CFRD in Campos Novos, Brazil, under the action of water pressure, the vertical joint of the concrete face slab in the riverbed was crushed and damaged, and the damage length reached 100 m, resulting in serious leakage, with a leakage rate as high as 1400 L/s[6].

Crack prevention in concrete face slabs constitutes a major challenge hindering the rapid development of high CFRDs in alpine regions. This is primarily attributed to the harsh climatic conditions prevalent in these areas, characterized by significant annual temperature variations, large diurnal temperature differences, extremely low temperatures, high wind speeds, and relatively low air humidity[10,11] . Under such conditions, concrete face slabs are susceptible to various deterioration mechanisms and cracking types, including freeze-thaw cycle damage [12] , thermal cracking [9,13,14] , drying shrinkage cracking [15] , and frost-heaving cracking [16] . Consequently, concrete face slabsin alpine regions exhibit a significantly higher propensity for cracking compared to those in temperate climates. Therefore, research on crack resistance technologies for CFRD face slabs in alpine regions has become a critical focus in dam engineering.

To mitigate the cracking problem in face slabs, extensive investigations have been undertaken, which can be broadly categorized into material improvement and structural design strategies. Recent developments in materials engineering have produced a wide range of strategies to enhance the crack resistance of hydraulic and structural concretes. Fiber reinforcement remains one of the most effective approaches. Basalt fiber, multi-scale polypropylene fiber and polypropylene macro fiber, for instance, can substantially improve early-age tensile strength, reduce shrinkage, and restrain thermal cracking through their three-dimensional network structure within the concrete matrix[17-19]. Similarly, steel fiber reinforcement has been proven to enhance fracture energy and post-cracking ductility, with optimal contents around 1.0-2.0 vol % delivering the best balance between tensile strength, toughness, and microstructural compactness in both geopolymer and desert-sand concretes[20,21]. Incorporating polymeric and rubberized materials introduces elasticity and energy absorption to otherwise brittle concrete. Waste rubber and zeolite composites, for example, show a strong synergistic effect: zeolite enhances the pozzolanic reaction and pore refinement, while rubber particles improve ductility and fracture energy, resulting in markedly better tensile–shear resistance and toughness[22,23]. Furthermore, aqua-thermal treatment of rubber aggregates combined with recycled tire steel fibers restores the interfacial bonding strength and transforms brittle fracture behavior into a more ductile response, significantly improving impact resistance and load-carrying stability[24]. At the micro- and nano-scale, hybrid systems that couple natural or synthetic fibers with nanomaterials have been found to exhibit pronounced improvements in crack mitigation. The combined addition of flax fibers and multi-walled carbon nanotubes enhances both the bridging capacity and microstructural integrity, reducing crack length by more than 80 % compared with plain concrete[25]. Similarly, the introduction of graphene tubes into rubberized matrices enhances hydration, stiffness, and fracture toughness due to strong nano-scale bonding and crack-bridging effects[26]. For hydraulic concretes, especially those used in alpine or cold regions, optimization of binder composition and modifier selection is also critical. Crumb-rubber-modified asphalt concrete demonstrates superior low-temperature crack resistance, achieving failure temperatures as low as -43° C,thus meeting the performance requirements for impermeable panels in cold-region dams[27]. The incorporation of functional admixtures is recognized as an effective strategy for enhancing the crack resistance of concrete. However, the efficacy and impact of these admixtures vary considerably depending on their specific mechanisms of action. While they may improve crack resistance, they can also exert unintended constraints on other critical properties of concrete, such as workability, mechanical strength, and durability. Traditional approaches for evaluating the crack resistance of concrete predominantly rely on single-index testing methods, such as the ring test, the plate test, or simple strength-based ratios. While these methods are straightforward and widely used, they suffer from fundamental limitations when applied to material selection or performance optimization. Single-index evaluations capture only one facet of a multi-dimensional problem. A concrete mixture may exhibit excellent compressive strength but poor drying shrinkage control, or high early-age tensile strain but severe autogenous deformation. In such cases, relying on any single indicator can lead to misleading or even contradictory conclusions.

Therefore, to address the challenges of material selection for alpine rockfill dams, this study adopted a systematic two-phase approach. Phase I established an optimized reference mix tailored for the YQ project by evaluating the effects of water-to-binder ratios and fly ash content on key performance indicators, including mechanical properties, tensile strain, drying shrinkage, and freeze-thaw resistance. Phase II involves investigation of the impact of various internal admixtures. To address the severe cracking risk of CFRD face slabs in alpine regions, five representative functional admixtures were selected based on their distinct mechanisms and documented effectiveness in coldclimate or shrinkageprone applications: NCC possesses ultrafine particles that fill capillary pores, refine the microstructure, and accelerate cement hydration. Its nucleation effect enhances early strength and reduces permeability. SF is a highreactivity pozzolan that significantly densifies the interfacial transition zone and improves mechanical strength and impermeability. However, its high specific surface area increases water demand and autogenous shrinkage. To offset this drawback, SFFA was also included, as the synergy between SF and FA can enhance workability, reduce shrinkage, and maintain longterm durability. MgO expansive agent produces controlled delayed expansion, which can compensate for thermal contraction and drying shrinkage, thereby generating precompressive stress under restraint. ACM is a proprietary composite consisting of nanoactive powder and highly dispersed synthetic fibers. It is designed to simultaneously enhance impermeability and crack resistance.

Table 1 Main chemical components of cement (wt%).

Compositions	CaO	SiO_2	Al_2O_3	Fe_2O_3	MgO	SO_3	f-CaO	loss	Insoluble substance	C_3S	C_3A
Cement	61.32	23.76	4.00	4.38	2.01	1.98	0.28	0.55	0.22	30.21	3.17

Table 2(a) Chemical composition of fly ash (wt%).

Compositions	SiO_2	Al_2O_3	Fe_2O_3	CaO	MgO	SO_3	f-CaO	Alkali content	Insoluble substance	C_3S	C_3A
Fly Ash	51.39	32.40	7.96	2.58	0.95	0.60	0.04	1.59	0.22	30.21	3.17

Table 2(b) Physical properties of fly ash (%).

Properties	Fineness (45 μm sieve residue)	Water demand ratio	Loss on ignition	Activity index
Fly Ash	8.7	94.9	1.32	80.2

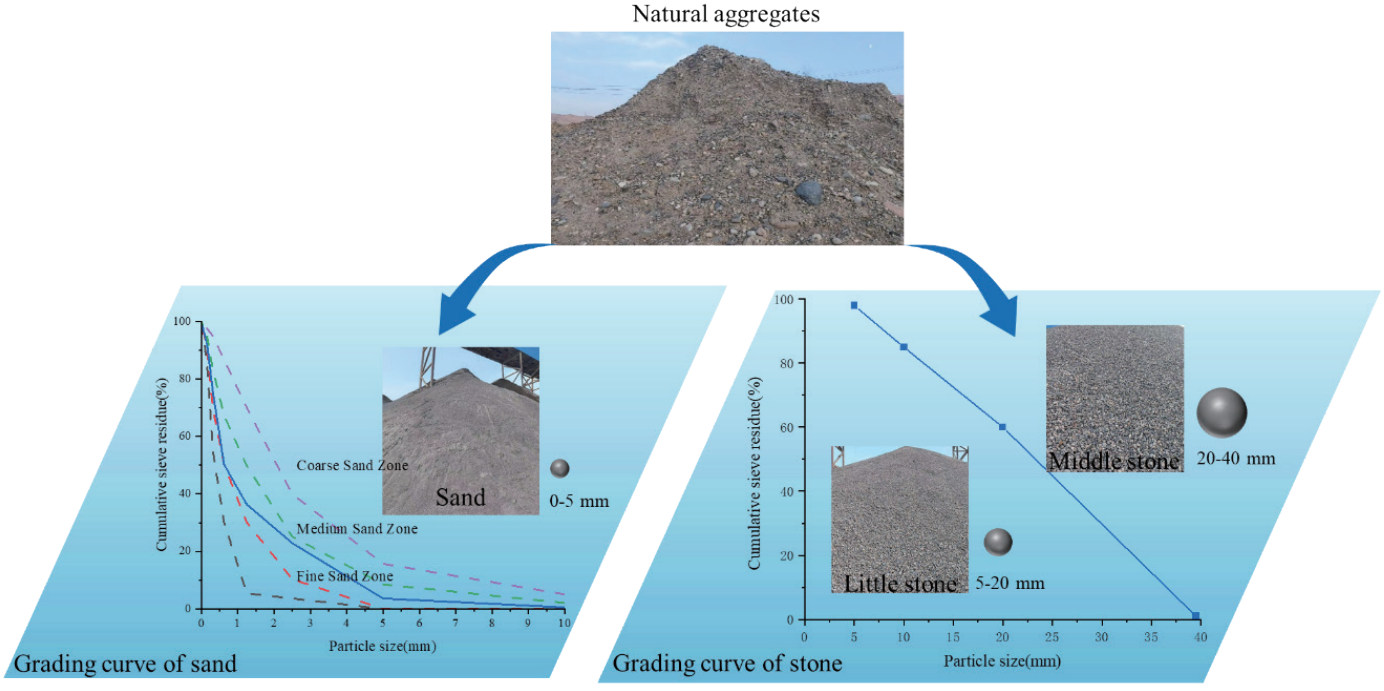

Fig. 1 Aggregates for the YQ rockfill dam project.

To overcome the limitations and inconsistencies of traditional single-index methods, an intelligent evaluation framework based on the EWM was developed which integrates multi-dimensional experimental data to quantify a comprehensive crack resistance index, enabling a data-driven selection of the optimal admixtures.

2. Materials and Experimental Methods

2.1 Raw materials

The experiment employed Portland moderate-heat cement (P · MH 42.5). The chemical composition of the cement are presented in Table 1. Fly ash was sourced from the location of the YQ rockfill dam project.the chemical composition and physical properties of fly ash is shown in Table 2. A MNF-I high-range water reducer and an MD-YQ air-entraining agent were utilized. Both coarse and fine aggregates used in the experiment were natural aggregates obtained from the quarry site of the rockfill dam project, screened and processed on-site. The coarse aggregates included some crushed large gravel, as shown in Figure 1.

2.2 Experimental design

2.2.1 Optimal mix proportion test

The face slab concrete is designed with a strength grade of C30, impermeability grade of W12, and frost resistance grade of F400. It employs a two-graded aggregate distribution and is designed for a 28-day curing period. The objective of mix design and optimization is to produce concrete that meets requirements for strength, workability, and durability, while also being economically viable. The mix design process, conducted in accordance with the DL 5330-2015 standard and referencing existing concrete test data, involves the following steps: mix proportion calculation, determination of the water-to-binder ratio, unit water content, sand ratio, admixture dosage, and trial mixing, adjustment, and finalization of the mix.

To reasonably control the binder content, the lower limit of the water-to-binder ratio was set at 0.35 for the experiments. Based on this, four water-to-binder ratios (0.35, 0.40, 0.45, and 0.50) and three fly ash incorporation rates (20%, 25%, and 30%) were selected for the optimization trials of the two-graded face slab concrete. Under the condition that concrete workability and air content requirements were met, key parameters such as unit water content, total binder content, admixture dosage, and optimal sand ratio were determined through trial mixing. Compressive strength tests were conducted on concrete specimens following curation of 7 days, 28 days, and 90 days.

Initially, trial mixes were prepared based on the preliminary calculated mix proportions. The workability of the fresh concrete was assessed based on slump, air content, bleeding, and segregation. Adjustments were made to the initially set water content, sand ratio, and admixture dosage as necessary. Subsequently, with the water-to-binder ratio and water content fixed, 4 to 5 different sand ratios were tested. The sand ratio was incrementally adjusted by 1% to 2% for each trial mix. The sand ratio corresponding to the maximum slump or the minimum VC value was identified as the optimal sand ratio. Finally, using this optimal sand ratio, further trial mixing was conducted, adjusting the water content until the workability of the concrete mixture met the requirements. The final mix proportions determined for the experimental study are summarised in Table 3.

Note: The mix proportion numbering system is defined as follows. Using M3520 as an example, the letters and

Table 3 Preliminary mix proportions for face slab concrete

Mix design number	Water-to-binder ratio	Fly ash content (%)	Total adhesive material (kg/m^3)	Sand content (%)	Water-reducing agent content (%)	Air-entraining agent content (%)	Sand (kg/m^3)	Little Stone (kg/m^3)	Middle Stone (kg/m^3)
M3520	0.35	20	342.9	39.0	0.5	0.080	735.6	575.2	575.2
M4020	0.40	20	310.0	39.5	0.5	0.075	752.5	576.3	576.3
M4520	0.45	20	273.3	40.0	0.5	0.075	776.3	582.2	582.2
M5020	0.50	20	252.0	40.5	0.5	0.070	790.5	580.7	580.7
M3525	0.35	25	340.0	39.0	0.5	0.080	735.6	575.3	575.3
M4025	0.40	25	310.0	39.5	0.5	0.070	750.6	574.8	574.8
M4525	0.45	25	277.8	40.0	0.5	0.070	770.8	578.1	578.1
M5025	0.50	25	252.0	40.5	0.5	0.070	788.9	579.5	579.5
M3530	0.35	30	328.6	39.0	0.5	0.080	741.9	580.2	580.2
M4030	0.40	30	300.0	39.5	0.5	0.075	756.6	579.4	579.4
M4530	0.45	30	266.7	40.0	0.5	0.075	778.6	584.0	584.0
M5030	0.50	30	240.0	40.5	0.5	0.070	798.4	586.5	586.5

digits, in sequential order, represent the following: M-Face slab concrete; 35-Water-to-binder ratio of 0.35; 20-Fly ash incorporation rate of 20%.

2.2.2 Concrete crack resistance test

Based on the recommended concrete mix proportion, NCC, SF, SF-FA, MgO, and ACM were incorporated separately. By varying only the type of admixture, we systematically compared the properties of the concrete, including its fresh state behavior, mechanical performance, shrinkage, and durability. Throughout the testing process, the total binder content was kept constant. An internal incorporation method was adopted, where the added materials replaced an equal mass of cement, ensuring the water-to-binder ratio remained unchanged.

Concrete specimens were prepared with the incorporation of NCC, SF, SF-FA, MgO, and ACM, respectively. These were compared with reference concrete (RC) specimens, and the specific mix proportions are shown in Table 4. Testing encompassed the workability of the fresh concrete, mechanical properties, frost resistance, and impermeability.

The NCC used had a particle size of 50-100 nm and was incorporated at 3% of the total binder mass. The addition of NCC significantly increased the demand for chemical admixtures: the water-reducing agent dosage increased from 0.5% to 1.2%, and the air-entraining agent dosage increased from 0.08% to 0.28%. SF particles are smaller than 1 μm, with an average particle size of approximately 100 nm, which is about 1/100 of the average diameter of cement particles. Its specific surface area ranges between 15,000-25,000 m^2/kg. The fine particles of SF possess high dispersibility and can effectively fill the spaces between cement particles, enhancing the density of the hardened paste. Incorporating SF also markedly increased the demand for chemical admixtures: the water-reducing agent dosage rose from 0.5% to 1.0%, and the air-entraining agent dosage increased from 0.08% to 0.13%. Although SF effectively improves the microstructure of hardened cement paste and concrete, its small particle size and large specific surface area lead to increased water demand as its incorporation rate rises, consequently increasing drying shrinkage and autogenous volume deformation. To mitigate these adverse effects, the most effective method is to combine SF with other pozzolanic materials or functional components, leveraging their complementary advantages to achieve better technical and economic outcomes. Common current practices include combining SF with ultra-fine slag or combining SF with fly ash. This experiment employed a SF-FA. In this case, the increase in chemical admixture dosage was significantly lower compared to using SF alone: the water-reducing agent dosage was 0.6%, and the air-entraining agent dosage was 0.1%.The dosages of each admixture were determined with reference to the relevant Chinese industry standards for hydraulic concrete, particularly DL/T 5330–2015 Specification for mix proportion design of hydraulic concrete.

Light-burned MgO, produced in a suspension kiln, was used as the micro-expansion material and incorporated internally into the reference concrete. During the hardening process of the concrete, it induces slight expansion, generating pre-compressive stress under restrained conditions, thereby enhancing the crack resistance of the concrete[28,29]. The selected ACM was a composite of nano-active powder and highly dispersed fibers in a 2:3 ratio. The incorporation rate of the nano-powder was 0.4 kg/m^3, and the volumetric incorporation rate of the fibers was 0.6 kg/m^3. Following the addition of this material, the dosage of the water-reducing agent decreased to 0.4%, and the air-entraining agent dosage decreased to 0.06%.

2.3 Test methods

2.3.1 Mix properties testing

For concrete with a maximum aggregate size not exceeding

Table 4 Concrete mix proportions with added materials.

Added materials	Water-to-binder ratio	Fly ash content (%)	Internal filler content	Water (kg/m^3)	Total Cementitious Materials (kg/m^3)	Sand content (%)	Water-reducing agent dosage (%)	Air-entraining agent dosage (%)
NCC	0.35	30.0	3.0%	115.0	329.0	39.0	1.2	0.28
SF	0.35	0.0	8.0%	115.0	329.0	38.0	1.0	0.13
SF-FA	0.35	20.0	3.0%	115.0	329.0	38.0	0.6	0.10
MgO	0.35	30.0	0.65%	115.0	329.0	39.0	0.6	0.08
ACM	0.35	30.0	0.04%	115.0	329.0	39.0	0.4	0.06
RC	0.35	30.0	-	115.0	329.0	39.0	0.5	0.08

40 mm and a slump range of 10 mm to 230 mm, the slump of the concrete mixture was determined using a slump cone, as shown in Figure 2.

2.3.2 Mechanical properties test

Cube specimens with dimensions of 150 mm × 150 mm × 150 mm were prepared. The compressive strength and splitting tensile strength tests were conducted using a compression testing machine, as shown in Figure 3. For the compressive test, the loading rate of the testing machine was set within the range of 18-30 MPa/min, while for the splitting tensile test, the loading rate was set between 1.8 and 3.6 MPa/min. The average value of three specimens was taken as the test result for both the compressive strength and splitting tensile strength of the concrete.

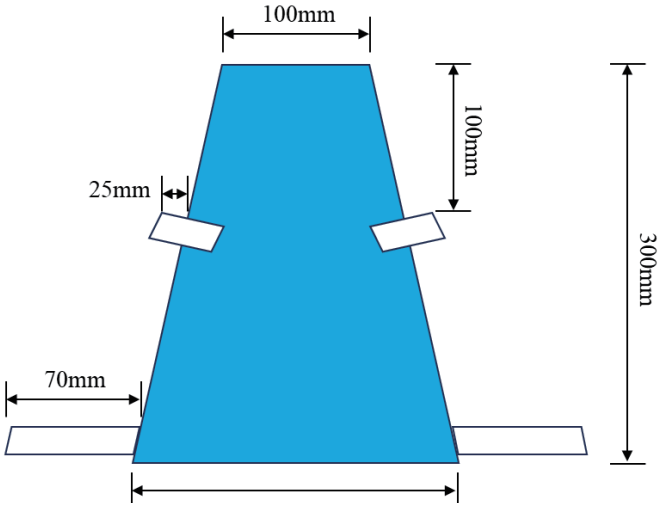

Fig. 2 Concrete slump test apparatus.

The compressive strength and splitting tensile strength of the concrete cubes are calculated using the equations below:

$$f_c = \frac{F_c}{A} \quad (1)$$

$$f_{ts} = \frac{2F_{ts}}{\pi A} \quad (2)$$

where f_c is the compressive strength of the concrete specimen (MPa); f_{ts} is the splitting tensile strength of the concrete specimen (MPa); F_c is the load applied during the compressive test (N); F_{ts} is the load applied during the splitting tensile test (N); A is the bearing area of the concrete specimen (mm^2), calculated as $A=150\times150\,mm^2$.

The elastic modulus of concrete was tested using cylindrical specimens measuring 150 mm in diameter and 300 mm in height. During the test, deformation was measured using displacement transducers with a gauge length of 150 mm. The elastic modulus of concrete was determined by fitting the slope of the obtained stress-strain curve.

2.3.3 Ultimate tensile strength test

The direct tensile tests were conducted in accordance with SL/T 352-2020, using large dumbbell-shaped prismatic specimens (550 mm total length, with a 100 mm × 100 mm midsection transitioning to 200 mm × 100 mm at the gripped ends). A tensile testing machine was used to apply a progressively increasing load until specimen failure, as shown in Figure 4.

2.3.4 Drying shrinkage performance test

The dying shrinkage performance test were conducted in accordance with GB/T 29417-2012. The drying shrinkage test for concrete was conducted using prismatic specimens measuring 100 mm × 100 mm × 500 mm. After casting, the specimens were demolded after 2 days, and their initial length was measured as the reference value. They were then transferred to a drying shrinkage laboratory for curing. To simulate the climatic conditions of alpine regions, the relative

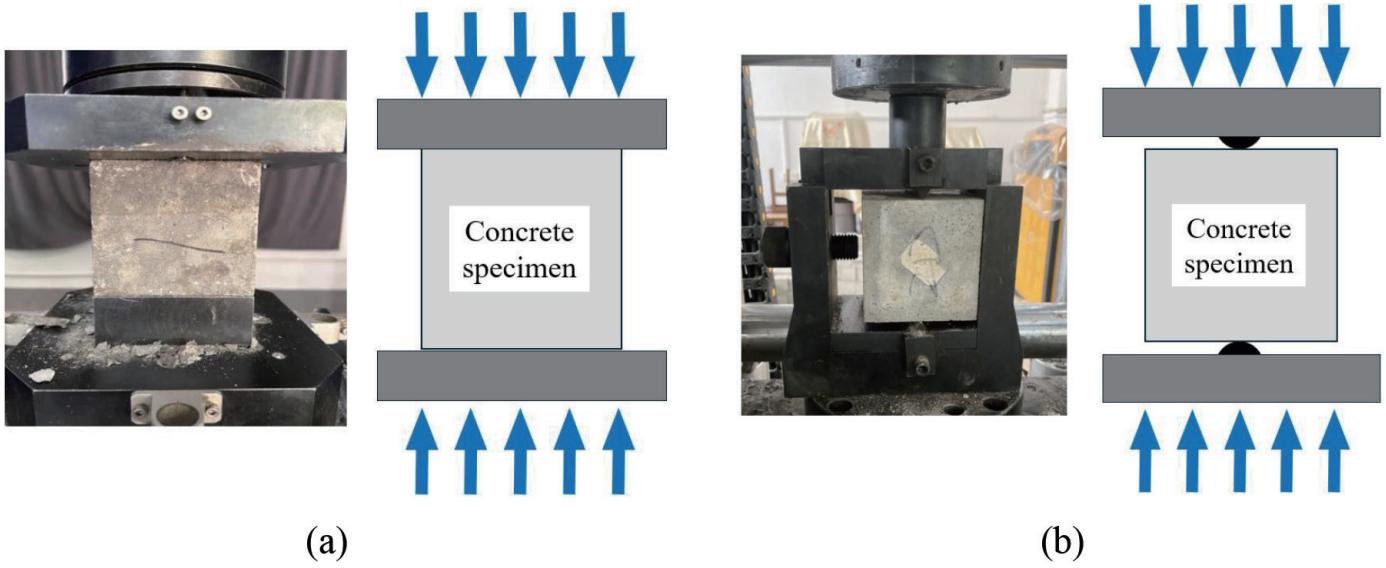

Fig. 3 Mechanical performance tests. (a) Compressive strength test; (b) Splitting tensile strength test.

humidity in the laboratory was maintained at 60% ± 5%. The drying shrinkage deformation was measured using dial gauges mounted on vertical drying shrinkage frames, as illustrated in Figure 5. After casting, concrete undergoes chemical shrinkage due to hydration reactions, leading to autogenous volume deformation. For the autogenous volume deformation test, cylindrical specimens measuring 150 mm in diameter and 500 mm in height were used. The concrete mixture was placed into the test molds equipped with embedded electrical resistance strain gauges at their centers. After compaction, the molds were immediately sealed and placed in a constant temperature room maintained at (20 ± 2)° C.The strain gauge readings taken 24 hours after casting were used as the reference values.

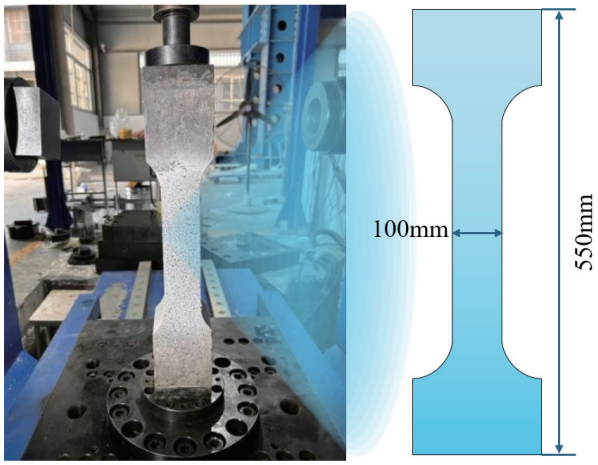

Fig.4 Tensile testing of concrete.

The drying shrinkage strain of concrete was calculated using Formula (3):

$$\varepsilon = \frac{l_t - l_0}{l_0} \times 100\% \quad (3)$$

Where ε is the drying shrinkage strain of the concrete at an age of t days; l_0 is the reference length of the specimen (mm); l_t is the measured length of the specimen at an age of t days (mm).

2.3.5 Permeability test

The impermeability test was conducted in accordance with the graded pressurization method specified in the SL/T 352-2020 standard. After the water pressure reached the predetermined value, it was maintained steadily for 8 hours. Subsequently, the specimens were removed and split to measure the water penetration depth. Finally, the impermeability grade of the concrete was determined based on the average penetration depth of six specimens. The test setup is shown in Figure 6.Formula (3):

The impermeability grade P of the concrete is calculated as below.

$$P = 10(H - 0.1) \quad (4)$$

Where P is the impermeability grade, and H is the lowest water pressure at which more than two of the six specimens exhibit water penetration.

2.3.6 Freeze resistance testing

The frost resistance test was conducted in accordance

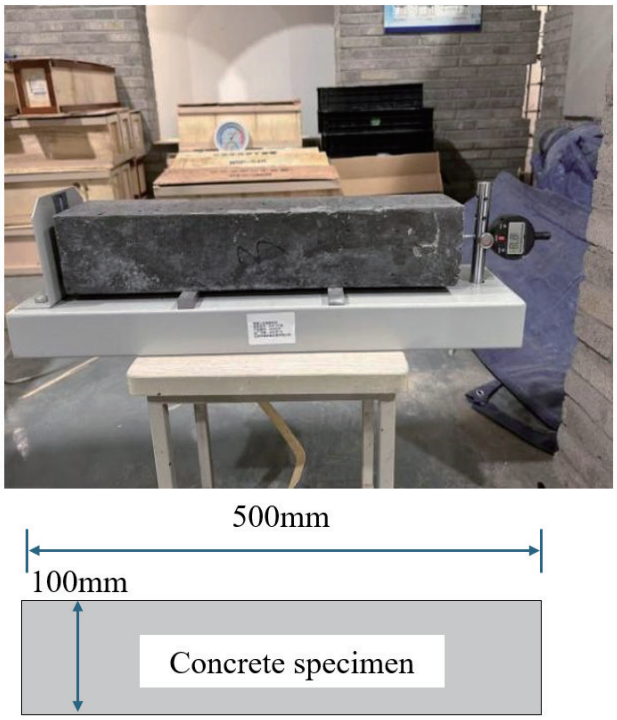

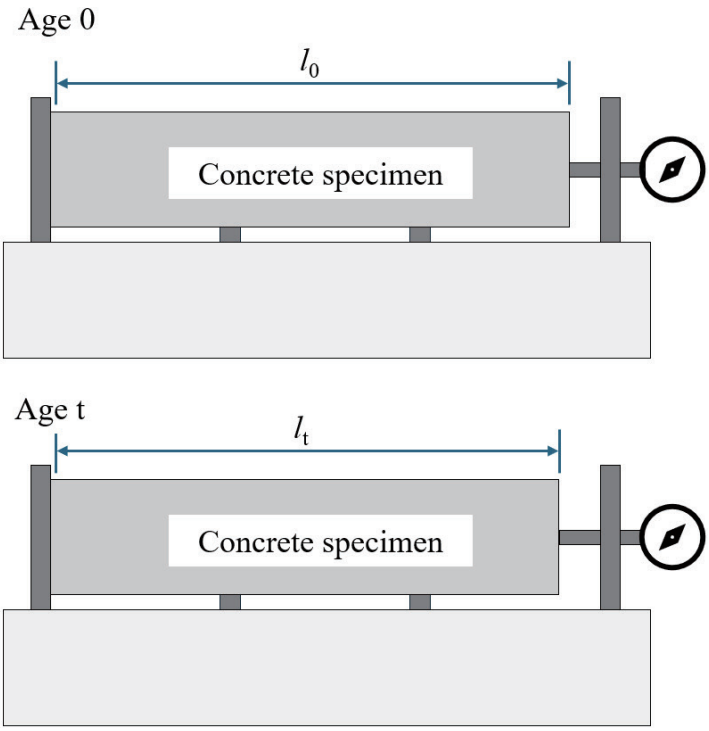

Fig.5 Drying shrinkage performance test of concrete.

with the rapid freezing-and-thawing method specified in the SL/T 352-2020 standard, using a fully automatic freezing-and-thawing testing apparatus. The concrete specimens measured 100 mm × 100 mm × 400 mm, and the inner walls of the test molds were lined with plastic film to facilitate demolding. During the test, the temperature at the center of the concrete specimens cycled between (-18 ± 2) ° C and (5 ± 2) ° C, with each complete freeze-thaw cycle lasting 2 to 4 hours.

The failure of concrete under freezing-and-thawing action was determined based on the relative dynamic elastic modulus and mass loss rate, both of which were measured every 25 cycles. The fundamental transverse frequency of the specimens was determined using the forced resonance method or impact resonance method, and the relative dynamic elastic modulus after multiple freeze-thaw cycles was calculated using Formula (2-6). Testing was terminated when the relative dynamic elastic modulus decreased to 60% or the mass loss rate reached 5%, at which point the specimen was considered to have failed. To ensure the frost resistance of the face slab concrete, an additional criterion was applied during testing: the relative dynamic elastic modulus of the concrete must not fall below 80% after the specified number of freeze-thaw cycles. The formulas for calculating the relative dynamic elastic modulus and the mass loss rate are given as Formulas (5) and (6), respectively.

$$P_n = \frac{f_n^2}{f_0^2} \times 100\% \quad (5)$$

$$W_n = \frac{G_0 - G_n}{G_0} \times 100\% \quad (6)$$

where: P_n is the relative dynamic elastic modulus of the specimen after n freeze-thaw cycles;F_n is the fundamental transverse frequency of the specimen after n freeze-thaw cycles;F_0 is the fundamental transverse frequency of the concrete specimen before freeze-thaw cycling;W_n is the mass loss rate of the concrete specimen after n freeze-thaw cycles;G_0 is the mass of the concrete specimen before freeze-thaw cycling;G_n is the mass of the concrete specimen after n freeze-thaw cycles.

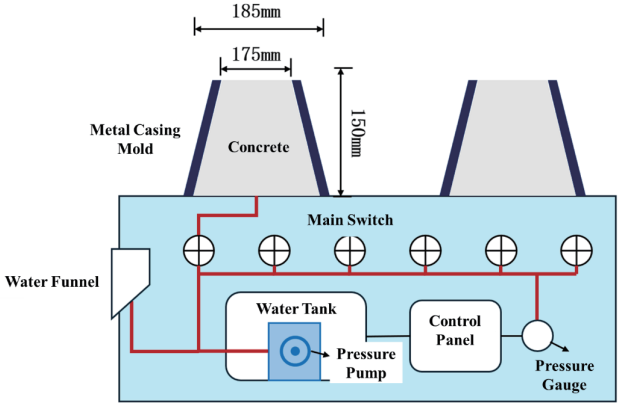

Fig.6 Concrete permeability test.

2.3.7 Early-age cracking testing

The early-age cracking resistance of concrete was evaluated using a restrained plate test based on the principles of CECS 13:2009 Standard test methods for fiber reinforced concrete. However, because the maximum aggregate size of the face slab concrete is 40 mm, the standard mold thickness (63 mm) was insufficient to avoid wet-sieving, which would alter the mortar content and bias the cracking assessment. Therefore, a custom-designed mold with internal dimensions of 600 mm × 600 mm × 100 mm was used. To provide uniaxial restraint against shrinkage, the perimeter of the mold is equipped with double rows of steel studs (Φ6, spacing 60 mm). The studs are arranged alternately with lengths of 50 mm and 100 mm to create a non-uniform restraint field that simulates realistic boundary conditions. The bottom surface of the mold is lined with double-layer PVC film to eliminate bonding and allow free shrinkage of the slab.

Immediately after casting, the mold (with specimen) is placed in a controlled environmental chamber maintained at 20 ± 2 ° C and 60 ± 5 % relative humidity.

An industrial fan(power >180 W) is positioned to generate airflow parallel to the specimen surface. The wind speed is adjusted to 5 ± 0.5 m/s, measured at a point 100 mm directly above the center of the slab. A schematic of the complete test setup is shown in Figure 7. After 24 hours of exposure, the surface of the specimen is examined. Crack length is measured with a steel ruler (straight-line distance between crack tips; curved cracks are measured segmentally). Crack width is measured using a crack width microscope with an accuracy of 0.01 mm. The total nominal crack area is calculated as the sum of the product of each crack’ s length and its corresponding maximum width. This integrated index reflects the combined effect of plastic shrinkage, autogenous shrinkage, and drying shrinkage, and is used to rank the early-age cracking resistance of different concrete mixtures.

Fig.7 Early-stage cracking test of concrete.3. Results and Discussion

3. Results and Discussion

3.1 Mix Proportion Performance Test Results

3.1.1The properties of the concrete mixture

The test results for the properties of the concrete mixture are summarized in Table 5. The data obtained suggest that the slump and air content of the mixture conform to the design requirements, with good cohesion and no significant bleeding observed.

Table 5 Test results for properties of mixtures with different mix proportions.

Code	Slump (mm)	Air content (%)	Bulk density (kg/m^3)	Setting time (h:min)	
				Initial setting time	Final setting time
M3520	85	5.5	2349	9:00	13:50
M4020	80	5.8	2339	9:30	14:10
M4520	70	5.5	2337	10:20	14:30
M3525	88	5.6	2345	10:50	15:40
M4025	88	6.0	2334	11:20	15:50
M4525	84	5.3	2330	11:20	15:30
M3530	90	5.7	2346	11:50	16:50
M4030	89	5.7	2336	12:50	15:30
M4530	90	6.0	2333	12:30	16:20

Table 6 Strength test results for concrete with different mix proportions.

Code	Compressive strength (MPa)			Splitting strength (MPa)		
	7d	28d	90d	7d	28d	90d
M3520	30.7	39.5	46.0	2.25	3.10	3.50
M4020	25.0	36.6	43.3	1.92	2.70	3.22
M4520	19.6	33.0	39.0	1.46	2.35	3.12
M3525	27.6	38.0	45.5	1.92	3.20	3.60
M4025	24.8	35.0	42.3	1.89	2.75	3.31
M4525	19.0	31.5	38.0	1.60	2.40	3.10
M3530	26.4	39.0	44.8	1.90	3.07	3.46
M4030	22.0	34.1	40.0	1.80	2.46	3.16
M4530	16.2	28.5	34.2	1.33	2.30	2.79

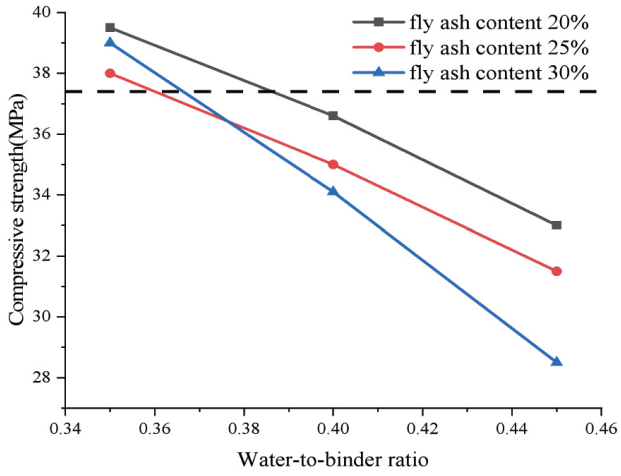

Fig.8 Concrete strength in 28-day. (a) Compressive strength; (b) Splitting tensile strength.

3.1.2 Mechanical Properties

It can be observed from the concrete test results from Table 6 that the 7-day compressive strength of all mix proportions is approximately 60% to 80% of the 28-day compressive strength, while the 90-day compressive strength reaches about 110% to 120% of the 28-day strength, indicating a normal strength development pattern. The ratio of splitting tensile strength to compressive strength across different ages ranges between 7% and 8.5%. The variations in 28-day compressive and splitting tensile strengths are illustrated in Figure8. According to the concrete strength design requirements, the specified characteristic strength of C30 concrete at a 95% assurance rate is 37.4 MPa. The observed enhancement in 28-day compressive strength (50.1 MPa) with SF incorporation is consistent with previous findings, which attributed this to the high pozzolanic activity and pore-filling effect of silica fume. Compared to the reference mix, the SF-modified concrete exhibited superior strength, aligning with the trends reported by Cheng Hu[30] for high-performance concrete. Accordingly, the corresponding water-to-binder ratio ranges were determined as follows: 0.35-0.38 for a fly ash content of 20%, 0.35-0.36 for a fly ash content of 25%, and 0.35-0.365 for a fly ash content of 30%. Notably, the 28-day splitting tensile strength of concrete with a fly ash content of 25% was higher than that of other fly ash incorporation levels. Based on a comprehensive analysis of all strength test results, a water-to-binder ratio range of 0.35-0.36 is recommended as reasonable.

3.1.3 Ultimate tensile strain

Analysis of the ultimate tensile strain results shown in Table 7 indicates that at a water-to-binder ratio of 0.35, the ultimate tensile strain of all concrete mixtures at 28 days exceeds 100×10^{-6}, meeting the standard requirements. As the water-to-binder ratio increases, the ultimate tensile strain of concrete gradually decreases, demonstrating that a lower water-to-binder ratio positively enhances the ultimate tensile performance of concrete.

Furthermore, an increase in fly ash content slightly reduces the ultimate tensile strain of concrete at 28 days. However, at a water-to-binder ratio of 0.35, the values still satisfy the standard specifications. In terms of long-term performance, the ultimate tensile strain at 90 days shows significant growth, and the influence of fly ash content becomes negligible at this stage. This suggests that fly ash primarily affects the early-age ultimate tensile strain of concrete, with no significant adverse effect on its long-term performance.

Table 7 Test results of ultimate tensile strength for concrete with different mix proportions.

Code	Ultimate tensile strain (10-6)			Growth rate based on 28d (%)		
	7d	28d	90d	7d	28d	90d
M3520	97	110	117	88	100	106
M4020	90	106	114	85	100	108
M4520	71	96	105	74	100	109
M3525	93	106	117	88	100	110
M4025	80	99	110	81	100	111
M4525	66	94	104	70	100	111
M3530	80	100	115	80	100	115
M4030	70	94	106	74	100	113
M4530	63	92	103	68	100	112

3.1.4 Drying shrinkage test results

The drying shrinkage test results of concrete (Figure 9) indicate that the 60-day drying shrinkage of the face slab concrete generally falls within the range of 400×10^{-6} to 500×10^{-6}. Variations in the water-to-binder ratio exhibit a relatively minor influence on the drying shrinkage of concrete. In contrast, the fly ash content demonstrates a significant effect on drying shrinkage performance-the higher the fly ash content, the lower the drying shrinkage rate of the concrete. This indicates that increasing the fly ash content is beneficial for controlling the drying shrinkage of concrete face slabs in alpine regions[31].

3.1.5 Test results for the impermeability

The test results for the impermeability of concrete as shown in Table 8 indicate that lower water-to-binder ratios and fly ash contents lead to reduced average penetration depths and accordingly improved impermeability. Concrete with a water-to-binder ratio of 0.35 demonstrated favorable impermeability, exhibiting an average penetration depth not exceeding 1.30 cm and a corresponding relative permeability coefficient of less than 2.9×10^{-5} cm/h.

3.1.6 Test results for the frost resistance

The test results for the frost resistance of concrete in Figure 10 show that after 400 freeze-thaw cycles, the relative dynamic elastic modulus of the M4530 group dropped below 80%, while that of all other groups remained above 80%. The mass loss rate for all groups was less than 5%. These findings indicate that the frost resistance of concrete specimens with higher water-to-binder ratios and higher fly ash content is significantly compromised under a high number of freeze-thaw cycles. In contrast, concrete mixtures with lower water-to-binder ratios and lower fly ash content exhibit satisfactory frost resistance after 400 cycles.

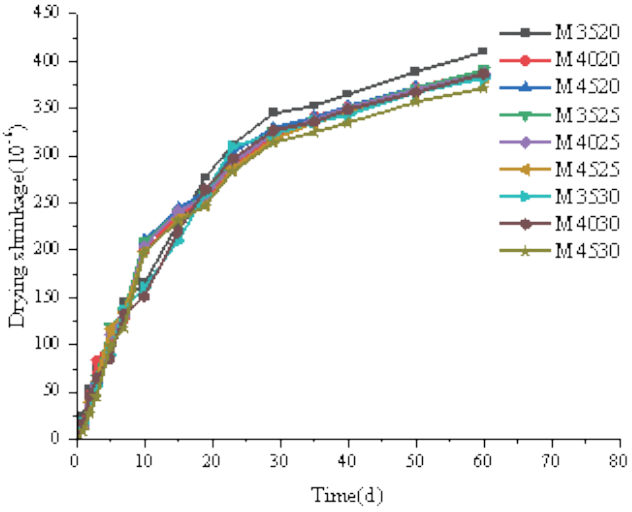

Fig.9 Drying shrinkage test results for concrete with different mix proportions.

Table 8 Test results of permeability resistance for concrete with different mix proportions.

Code	Maximum Water Pressure (MPa)	Average penetration height (cm)	Relative permeability coefficient (cm/h)	Water Resistance Grade
M3520	1.3	1.11	2.1×10-5	>W12
M4020	1.3	1.23	2.6×10-5	>W12
M4520	1.3	1.65	4.6×10-5	>W12
M3525	1.3	1.20	2.5×10-5	>W12
M4025	1.3	1.58	4.3×10-5	>W12
M4525	1.3	1.73	5.1×10-5	>W12
M3530	1.3	1.30	2.9×10-5	>W12
M4030	1.3	1.58	4.3×10-5	>W12
M4530	1.3	1.77	5.4×10-5	>W12

3.1.7 Early-age cracking performance

The early-age cracking test results for the various mix proportions are summarized in Table 9. The test results indicate that all optimized mix proportions exhibited a relatively small number of cracks, suggesting an overall controllable cracking risk. Variations in the fly ash content had a minor influence on the total nominal crack area, whereas the total nominal crack area increased significantly when the water-to-binder ratio exceeded 0.40. Both the maximum crack length and maximum crack width increased gradually with an increase in the water-to-binder ratio, indicating that a lower water-to-binder ratio is beneficial for early-age crack control. Furthermore, the total nominal crack area showed an increasing trend with high fly ash content, while a low fly ash content contributes positively to the inhibition of early-age cracking.

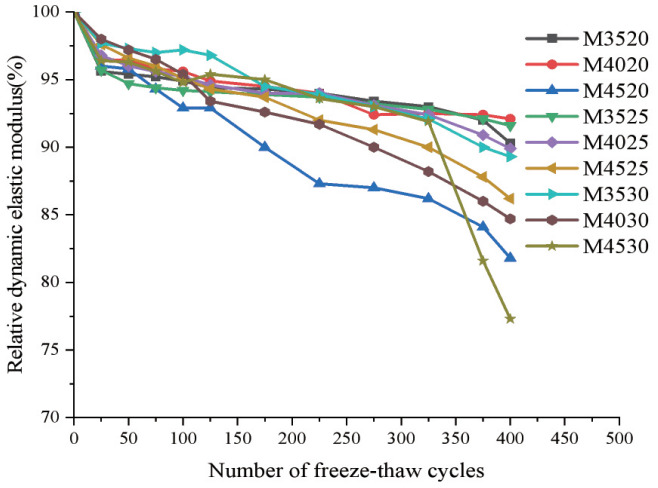

(a)

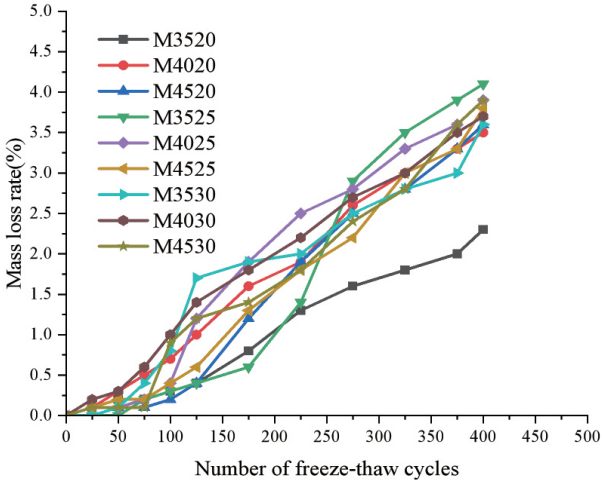

(b)

Fig. 10 Test results for the frost resistance of concrete. (a) Relative dynamic elastic modulus; (b) Mass loss rate.

Table 9 Test results of the early-age cracking performance.

Code	Number of cracks	Maximum crack length (mm)	Maximum crack width (mm)	Total area of cracks (mm^2)
M3520	3	160	0.2	59
M4020	3	170	0.2	104
M4520	4	220	0.3	144
M3525	3	150	0.2	60
M4025	3	180	0.3	88
M4525	5	280	0.3	152
M3530	3	190	0.2	75
M4030	5	200	0.3	165
M4530	6	270	0.3	198

3.1.8 Optimal mix proportion

The test results indicate that an increase in fly ash content adversely affects the mechanical properties, early-age ultimate tensile strain, impermeability, and early-age crack resistance of concrete, while it beneficially reduces the drying shrinkage. Comprehensive comparison shows that concrete with fly ash contents of 20% and 25% exhibits superior overall performance. Increasing the fly ash content from 20% to 30% does not significantly alter the concrete properties, and all mixtures within this range satisfy the engineering requirements. Since the incorporation of fly ash significantly reduces cement consumption, contributing substantially to cost control, a fly ash content of 20% to 30% is recommended. Thus, the specific value should be selected based on the performance requirements and budget constraints of the actual project.

Furthermore, the water-to-binder ratio considerably influences the mechanical strength of concrete, with higher ratios leading to a gradual decline in mechanical performance. To meet the specified C30 strength requirement while utilizing the recommended fly ash content (20%-30%), the water-to-binder ratio should be controlled within the range of 0.35 to 0.36. The final recommended mix proportions for the face slab concrete are summarized in Table 10.

3.2 Effects of different admixtures on concrete properties

3.2.1 The properties of the concrete mixture

The test results for the properties of fresh concrete

Table 10 Recommended mix proportions for face slab concrete.

Water-binder ratio	Fly ash content (%)	Total Binder (kg/m^3)	Sand ratio (%)	Water reducer content (%)	Air-entraining agent content (%)
0.35-0.36	20-30	329-343	39	0.5	0.08

are presented in Table 11, and the workability comparison is illustrated in Figure 11. The results revealed that the incorporation of NCC significantly increased the viscosity of the concrete mixture, improved cohesion, and effectively suppressed bleeding and segregation. However, the slump increased to 70 mm, the highest among all groups, while the initial and final setting times were shortened by 3-4 hours. The mixture with SF also exhibited increased viscosity, but the slump decreased to 40 mm, the lowest among the six mixtures. The air content was 5.2%, also the lowest, and the initial and final setting times were reduced by 2-3 hours. The mixture with the SF-FA showed improved cohesion compared to the mixture with SF alone, and the setting times were shortened by 1-3 hours. The addition of MgO expansive material resulted in good cohesion of the mixture, with no bleeding or segregation, and a slight reduction in setting times. The mixture with the anti-seepage and crack-resistant material also demonstrated good cohesion, with a slump of 54 mm and a slight shortening of the setting times compared to the reference concrete.

According to the standard specifications, the slump of concrete mixtures should be in the range of 50 mm to 70 mm, and the air content should be between 4.5% and 6.5%. The properties of mixtures incorporating NCC, SF-FA, MgO, and ACM all met the standard requirements. In contrast, the mixture with SF alone exhibited a lower slump, which did not comply with the standard specification.

Table 11 Properties of concrete mixes with different admixtures.

Admixtures	Slump	Air content	Bulk density	Setting time (h:min)	
	(mm)	(%)	(kg/m^3)	Initial setting time	Final setting time
NCC	70	5.5	2350.0	8:00	12:30
SF	40	5.2	2380.0	9:30	13:00
SF-FA	55	5.3	2360.0	10:00	13:30
MgO	50	5.6	2340.0	10:10	15:30
ACM	54	5.5	2350.0	10:20	15:20
RC	68	5.7	2340.0	11:00	16:00

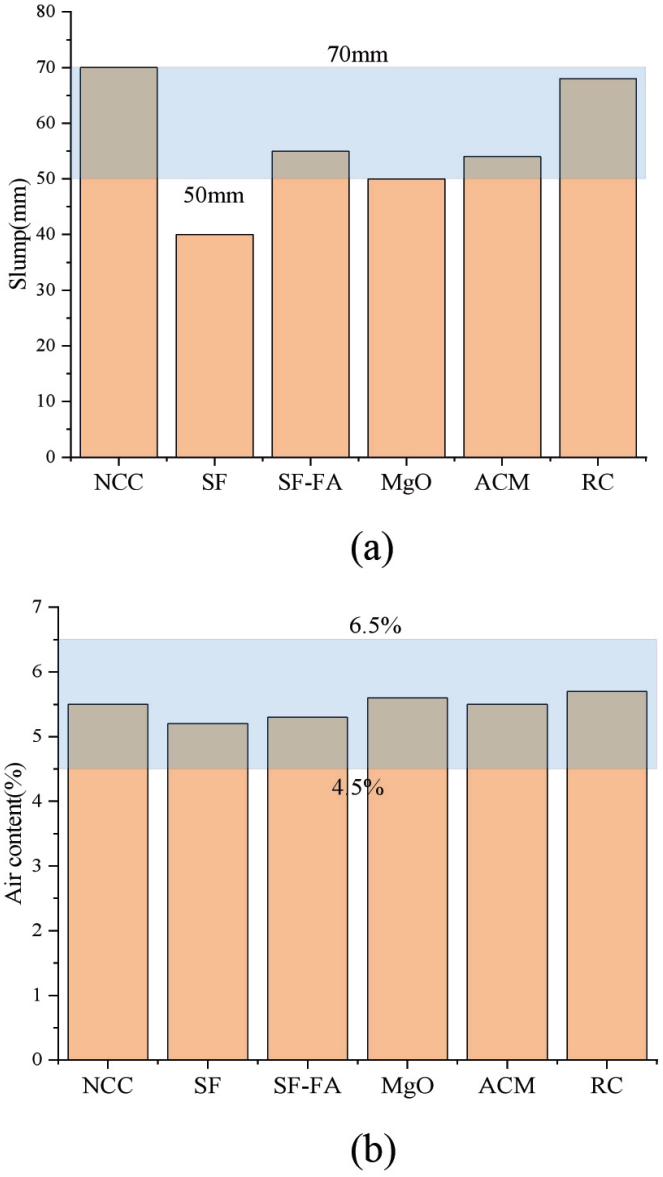

Fig.11 Concrete workability. (a) Slump; (b) Air content.

3.2.2 Mechanical Properties

The test results for compressive strength and splitting tensile strength are presented in Table 12. The measured strength values at 28 days are illustrated in Figure 12. The test results indicate that the mechanical strength of concrete gradually increases with age, with a long-term strength growth rate ranging from 10.0% to 19.0%. The concrete incorporated

with SF exhibited the highest compressive and splitting tensile strengths; however, its long-term compressive strength growth rate was relatively low. In contrast, the concrete with MgO showed lower compressive and splitting tensile strengths at all ages compared to the reference concrete, failing to achieve the intended improvement in concrete strength. The concrete incorporated with all other functional materials demonstrated higher compressive and splitting tensile strengths than the reference group, indicating a positive effect on concrete strength development. Under the requirement of a 95% strength assurance rate, the specified 28-day characteristic strength for C30 concrete is 37.4 MPa. The concrete mixtures incorporating NCC, SF, SF-FA, and ACM all met this strength requirement. However, the concrete with MgO exhibited insufficient mechanical performance and failed to satisfy the specified requirements.

Table 12 Mechanical strength of concrete with different admixtures.

Admixtures	Compressive strength (MPa)			Splitting strength (MPa)		
	7d	28d	90d	7d	28d	90d
NCC	28.7	39.4	46.7	2.02	3.18	3.54
SF	38.8	50.1	55.0	3.41	4.04	4.40
SF-FA	26.0	39.6	44.6	2.06	3.13	3.55
MgO	22.8	34.5	40.9	1.64	2.38	2.88
ACM	31.5	42.9	49.0	2.19	3.38	3.65
RC	26.0	38.4	44.0	1.84	3.00	3.42

3.2.3 Modulus of elasticity

The test results for the elastic modulus are summarized in Table 13, and the variation in the 28-day elastic modulus is shown in Figure 13. The results indicate that the concrete with SF-FA maintained a higher elastic modulus across all testing ages. The concrete incorporated with MgO exhibited a slightly higher elastic modulus than the reference concrete at early ages, but it gradually became lower than that of the reference concrete beyond 28 days. This phenomenon can be attributed to the dual effect of MgO hydration. Initially, the formation of magnesium hydroxide generates controlled micro-expansion, which may densify the matrix and enhance early stiffness, as reflected in the slightly higher initial elastic modulus. However, over a longer duration, if the expansive stress is not perfectly compensated or if it leads to the formation of localized micro-cracks or alters the pore structure unfavorably, it can compromise the overall integrity and load-transfer efficiency of the cement paste, resulting in a reduction of the long-term elastic modulus[32-34]. In contrast, the elastic modulus of concrete with all other added materials showed some degree of improvement compared to the reference concrete. This consistent improvement is primarily due to the persistent pore-refining and microstructure-densifying effects of these materials. SF and NCC, with their high surface area and nano-scale particles, effectively fill capillary pores and improve the interfacial transition zone, leading to a stiffer and more homogeneous matrix that resists deformation under load, thereby increasing the elastic modulus throughout the testing period [35,36].

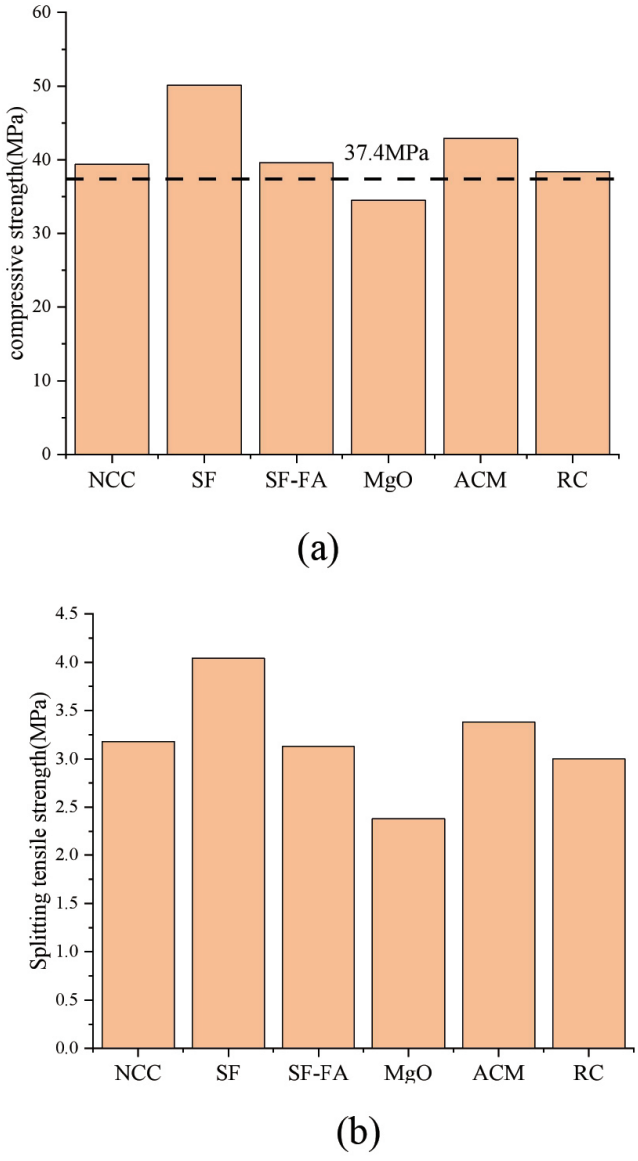

Fig.12 Concrete 28-day strength. (a) Compressive strength; (b) Splitting tensile strength.

3.2.4 Ultimate tensile strain

The ultimate tensile performance of concrete was tested using large dumbbell-shaped prismatic specimens. During testing, deformation was measured using clamps and displacement transducers with a gauge length of 200 mm. The tensile elastic modulus was determined as the slope of the fitted straight line for the stress-strain relationship within the

0–50% stress range of the failure stress. The test results for the ultimate tensile strain of concrete are presented in Table 14, and the variation in the 28-day ultimate tensile strain is shown in Figure 14. The results demonstrate that the ultimate tensile strain of concrete gradually increases with age, showing a growth range of 11.0%-27.0% at 90 days compared to the 28-day values. The incorporation of NCC, SF, SF-FA, and ACM all led to an increase in the ultimate tensile strain compared to the reference concrete, indicating that the addition of these materials is beneficial for enhancing the crack resistance of concrete. The most significant improvement in ultimate tensile strain was observed in concrete with SF, primarily due to its role in enhancing the internal compactness of concrete and reducing the formation of internal pores[37-40]. In contrast, the internal incorporation of MgO expansive material resulted in a slight reduction in the ultimate tensile strain, with values decreasing by 3.0%-6.0% compared to RC across all ages, indicating that the addition of MgO expansive material does not significantly improve the crack resistance of concrete.

Table 13 Elastic modulus of concrete with different admixtures.

Admixtures	Elastic modulus (GPa)		
	7d	28d	90d
NCC	27.3	30.9	35.0
SF	28.3	31.9	35.5
SF-FA	31.6	32.7	36.7
MgO	26.6	29.0	33.3
ACM	26.4	30.4	34.2
RC	26.4	29.9	34.7

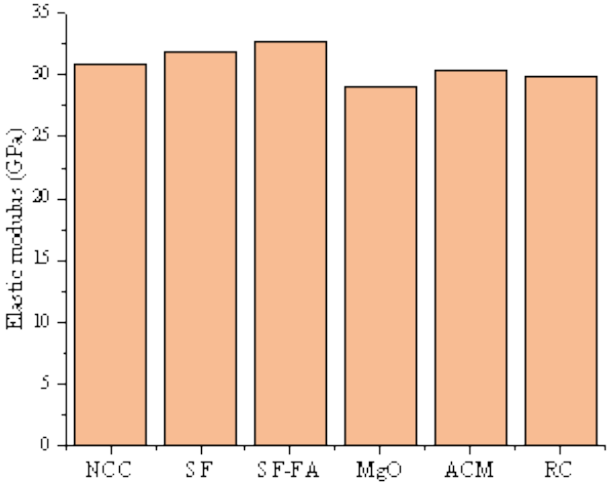

Fig.13 28-day elastic modulus of concrete.

Table 14 Ultimate tensile strength of concrete with different admixtures.

Admixtures	Ultimate tensile strength (10-6)			Growth rate based on 28d (%)		
	7d	28d	90d	7d	28d	90d
NCC	92.0	102.0	121.0	90.0	100.0	119.0
SF	104.0	111.0	127.0	94.0	100.0	114.0
SF-FA	81.0	115.0	128.0	70.0	100.0	111.0
MgO	69.0	85.0	108.0	81.0	100.0	127.0
ACM	75.0	93.0	115.0	81.0	100.0	124.0
RC	71.0	90.0	111.0	79.0	100.0	123.0

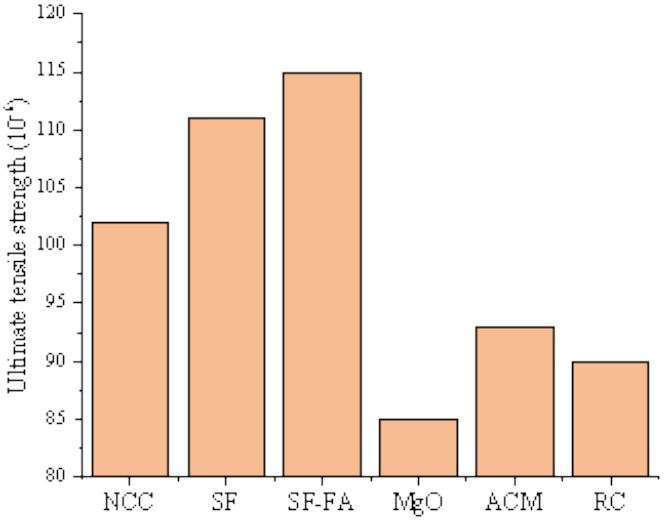

Fig.14 Ultimate tensile strength of concrete at 28 days.

3.2.5 Shrinkage properties

The test results for the drying shrinkage of concrete as shown in Figure 15 indicate the drying shrinkage strain of concrete increases with age, with the rate of increase being more pronounced at early ages. It can be observed that after 42 days, the growth trend gradually stabilizes, and by day 90, the range of concrete drying shrinkage strain is . Compared to RC, the incorporation of NCC or ACM reduces the drying shrinkage strain of concrete, while the addition of other materials increases the shrinkage deformation to varying degrees. Therefore, under the low-humidity conditions typical of alpine regions, the use of NCC or ACM can effectively mitigate the development of drying shrinkage in concrete.

The test results for autogenous volume deformation are presented in Figure 16. The incorporation of MgO expansive material resulted in a slight expansion of the concrete, reaching

by 90 days. This expansion can generate pre-compressive stress within the concrete under restrained conditions, effectively inhibiting cracking and positively contributing to the crack resistance of the concrete. In contrast, the addition of SF led to higher autogenous shrinkage deformation compared to the reference concrete, indicating that SF induces greater chemical shrinkage during the hydration process, which adversely affects the improvement of concrete crack resistance. Although the concrete incorporated with NCC, the SF-FA, and ACM still exhibited shrinkage behavior, the values were lower than those of the reference concrete, suggesting that these materials provide some improvement to the crack resistance of concrete.

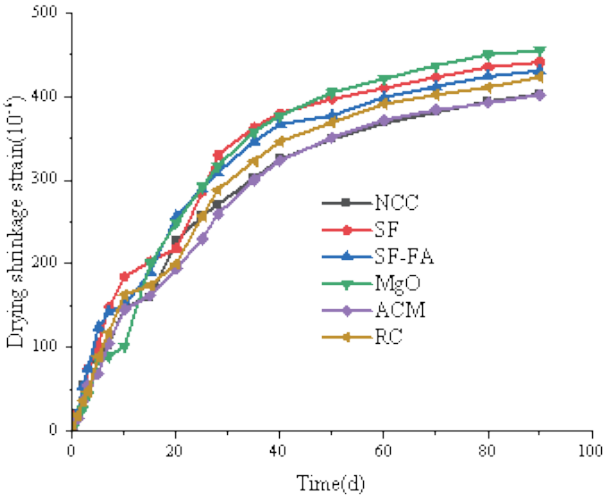

Fig.15 Drying shrinkage properties of concrete.

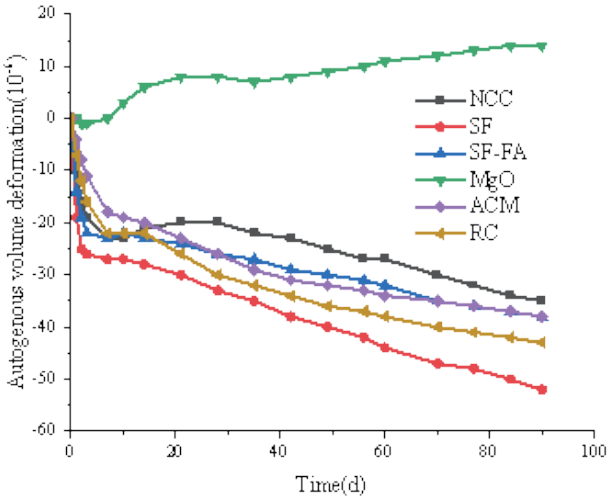

Fig.16 Autogenous volume deformation of concrete.

3.2.6 Durability

The test results for concrete impermeability and frost resistance are presented in Table 15 and Figure 17. The impermeability tests demonstrate that under the maximum water pressure of 1.3 MPa, the average penetration depth of concrete specimens incorporated with various functional materials was lower than that of the reference group, with all mixtures meeting the impermeability grade requirements. Notably, specimens containing the ACM exhibited the lowest average penetration depth, indicating the most effective impermeability. The frost resistance tests revealed that after 400 freeze-thaw cycles, the concrete specimens incorporated with NCC, SF, SF-FA, MgO, and ACM all showed superior performance in both relative dynamic elastic modulus and mass loss rate compared to the reference concrete. It is worth noting that the specimens with SF, SF-FA, and ACM exhibited a reduction in relative dynamic elastic modulus of less than 10% and a mass loss rate below 3%, demonstrating that these materials significantly enhance the concrete's resistance to freeze-thaw cycles. However, for specimens containing MgO expansive material, the relative dynamic elastic modulus decreased rapidly after exceeding 325 cycles, with the reduction exceeding 20% after 400 cycles. This indicates that the incorporation of MgO expansive material compromises the long-term frost resistance of concrete.

Table 15 Permeability test results for concrete with different admixtures.

Admixtures	Maximum water pressure (MPa)	Average penetration height (cm)	Water resistance grade
NCC	1.3	1.6	>W12
SF	1.3	1.5	>W12
SF-FA	1.3	1.5	>W12
MgO	1.3	2.6	>W12
ACM	1.3	1.2	>W12
RC	1.3	4.7	>W12

4. EWM Evaluation Model of Cracking Resistance Index

The crack resistance of concrete cannot be effectively evaluated by a single performance indicator alone, as its anti-cracking efficacy depends on the synergistic effects of multiple parameters. Generally, the crack resistance of concrete is positively correlated with its tensile strength and creep behavior, while it is negatively correlated with elastic modulus, coefficient of linear expansion, temperature rise, drying shrinkage, and autogenous volume deformation. The evaluation methods for the crack resistance of concrete have evolved from single-index approaches toward multi-index comprehensive assessment. Early research primarily relied on single-index methods, such as the ring test to determine the time to cracking under restrained conditions[41] , or the slab test to quantify the total area and width of early-age plastic

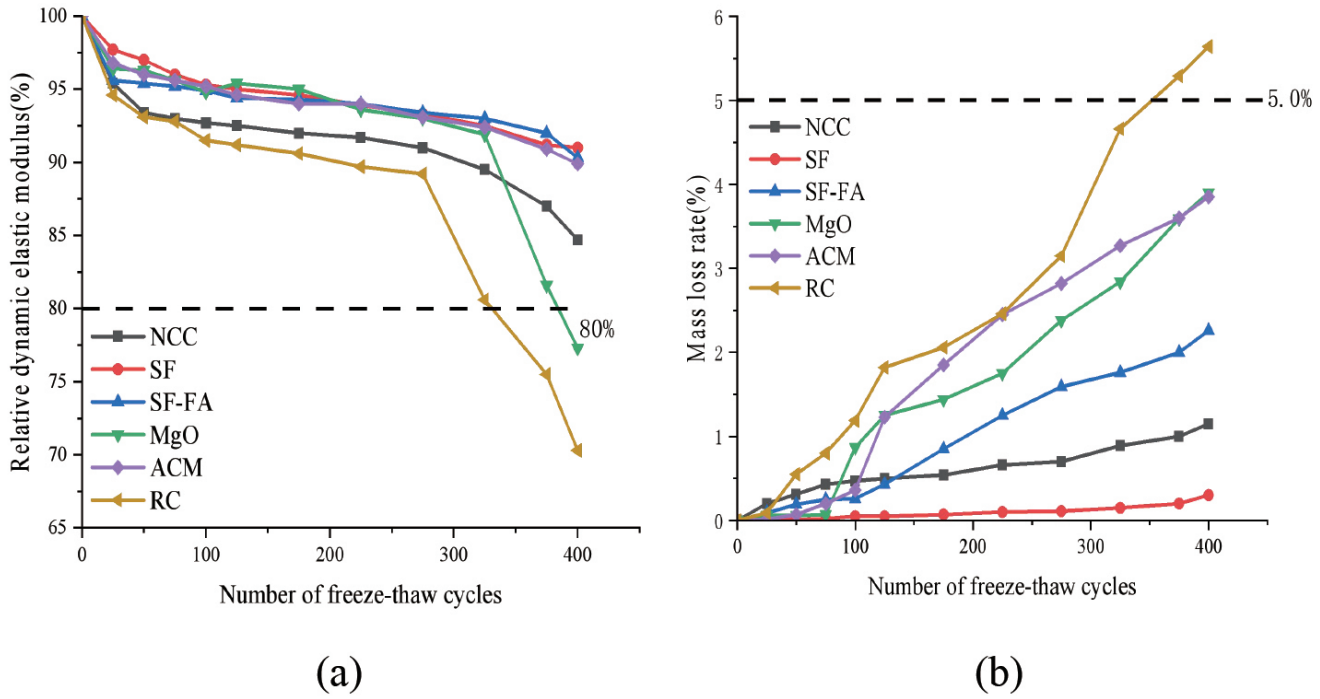

Fig.17 Freeze resistance of concrete. (a) Relative dynamic modulus (b) Mass loss rate.

shrinkage cracks[42]. While these methods are straightforward to perform, they often fail to comprehensively reflect the crack resistance of concrete under complex stress states. To enable a more holistic evaluation of crack resistance, researchers have proposed the use of a cracking resistance index by integrating fundamental parameters such as elastic modulus, tensile strength, shrinkage strain, and creep[43-45]. This index serves to quantitatively assess the relative ability of the material to resist cracking.

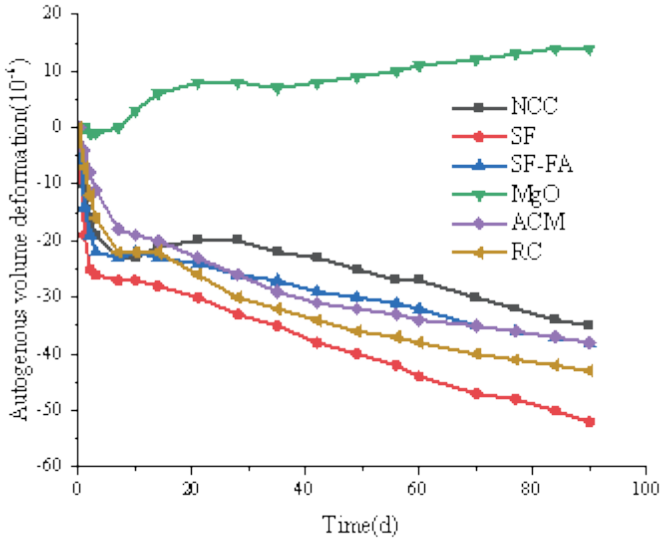

Fig.16 Autogenous volume deformation of concrete.

Drawing upon extensive experience in hydraulic concrete engineering, various formulations for the crack resistance index have been proposed. These formulas integrate critical parameters such as ultimate tensile strain, tensile strength, elastic modulus, autogenous volume deformation, adiabatic temperature rise, and drying shrinkage, as shown in Eq. (7). However, these formulas exhibit varying emphases on specific parameters, resulting in inconsistent evaluation outcomes that hinder the standardized assessment of the crack resistance enhancement provided by internal admixtures. To address this, a weighted multi-criteria evaluation model was constructed. To eliminate subjective bias, the Entropy Weight Method (EWM) was employed to objectively determine the contribution weights of the disparate crack resistance indices, thereby synthesizing the complex analytical results into a unified intelligent score.

$$I_{cr}=\begin{cases}\dfrac{R_L*\varepsilon_p}{E_L*\varepsilon_s} & [46]\\ \dfrac{R_L\left(\dfrac{1}{E_L}+C\right)}{\alpha T_r-G} & [47]\\ \dfrac{\varepsilon_p+CR_L+G}{\alpha T_r+\varepsilon_s} & [48]\end{cases} \tag{7}$$

Where R_L is the axial tensile strength of concrete;ε_p is the ultimate tensile strain of concrete;E_L is the tensile elastic modulus of concrete;ε_s is the drying shrinkage strain of concrete.C is the specific creep of concrete, 10^{-6}/MPa;G is the autogenous volume deformation, 10^{-6};α is the coefficient of linear thermal expansion 10^{-6}/℃ ; T_r is the hydration temperature rise of concrete, ℃ .To eliminate the dimensional differences among various formulas of Cracking Resistance Index, a min-max normalization technique was employed to map the raw data into a dimensionless interval [0, 1]. For each crack index in different formulas:

$$x'_{ij} = \frac{x_{ij} - \min(x_j)}{\max(x_j) - \min(x_j)} \quad (8)$$

To avoid subjective bias in coefficient selection, the EWM based on information theory was introduced. This algorithm objectively calculates the weights by analyzing the dispersion of the Cracking Resistance Index in different formulas, thereby assigning higher weights to indicators with greater variation.

The H_j entropy and weight w_j of the j-th indicator are calculated as:

$$H_j = -k\sum_{i=1}^{n} p_{ij}\ln(p_{ij}), \text{where } k = \frac{1}{\ln(n)} \quad (9)$$

$$w_j = \frac{1 - H_j}{\sum_{j=1}^{m}(1 - H_j)} \quad (10)$$

Finally, the Comprehensive Crack Resistance Index (CCRI) was established using a weighted linear combination model:

$$CCRI_i = \sum_{j=1}^{m} w_j \cdot x'_{ij} \quad (11)$$

This model transforms the multi-dimensional formulas into a single quantitative score, enabling an intelligent ranking of the admixture effectiveness. Where w_j represents the weighting factor derived from the sensitivity analysis of different formulas, and P_i represents the normalized performance indicators. This mathematical construct serves as a predictive algorithm to quantify the potential capability of concrete cracking resistance.

The superiority of the EWM-based evaluation over traditional methods lies in its comprehensive integration of conflicting performance metrics. Traditional evaluation approaches typically rely on a single criterion, such as the tensile strength-to-modulus ratio or specific shrinkage limits. However, concrete crack resistance in face slabs is a multi-physics problem involving mechanical strength, thermal evolution, and time-dependent deformation. As shown in our results, while certain admixtures significantly improve one aspect, they may simultaneously exacerbate others. The proposed composite index CCRI effectively penalizes high-risk traits and rewards synergistic improvements. This holistic perspective is particularly valuable for alpine CFRDs, where the selection of the optimal admixture combination must balance early-age thermal stresses with long-term drying shrinkage. Consequently, the EWM model offers a more robust decision-making tool for material optimization than conventional empirical methods.

The CCRI values derived from the EWM evaluation model are presented in Figure 18. The quantitative results indicate that SF, NCC, SF-FA, and MgO rank as the top four performers in crack resistance. Nevertheless, regarding fresh

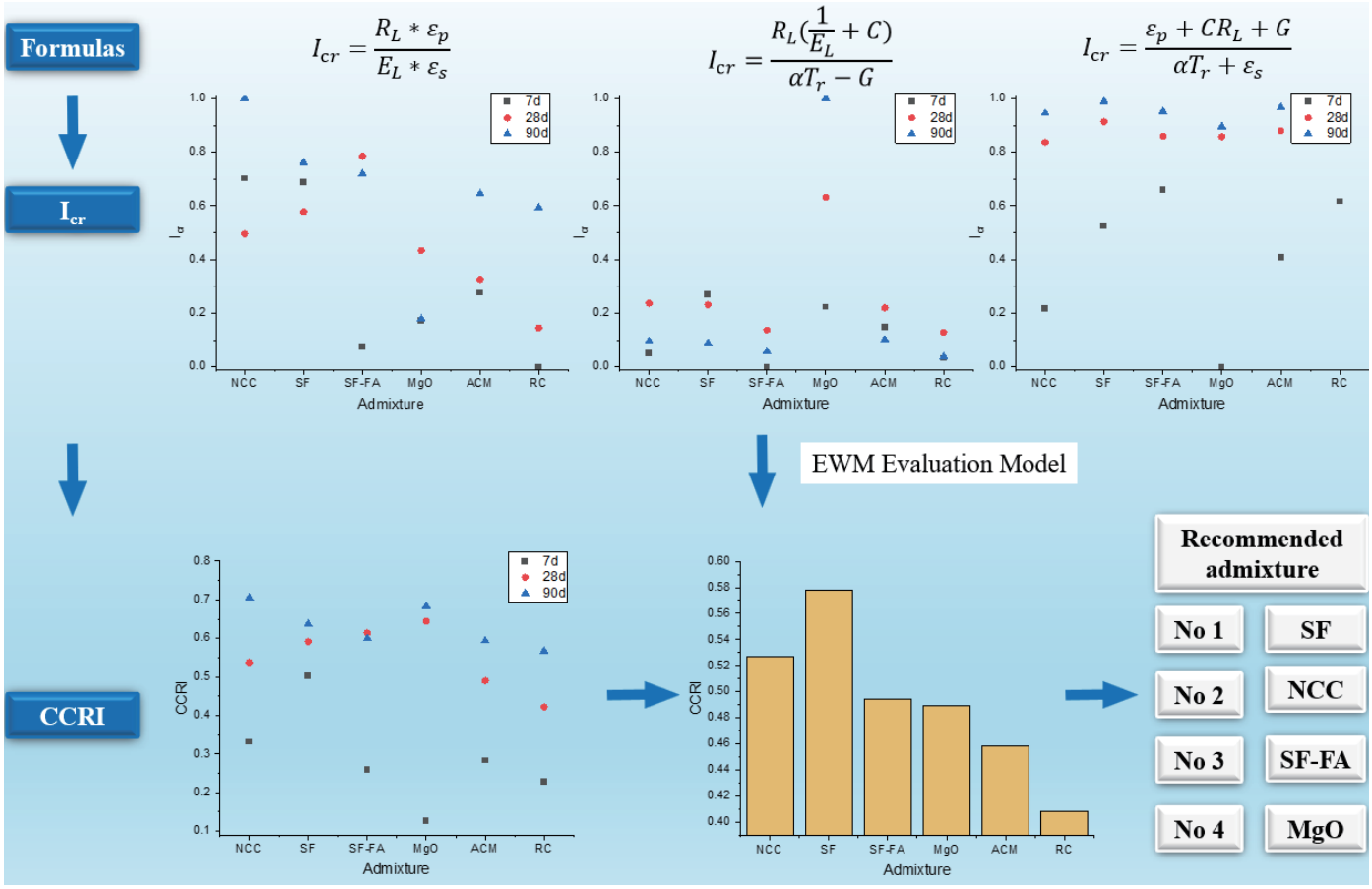

Fig.18 CCRI results from the EWM evaluation model.

concrete properties, the mixture with SF alone exhibited a lower slump, which did not comply with the standard specification. Therefore, balancing mechanical efficiency with constructability, NCC is selected as the preferred material to improve concrete performance.

5. Conclusion

The following conclusions are drawn from this study:

(1) An optimal concrete mix proportion for the face slabs of the YQ project in an alpine environment was successfully determined: a water-to-binder ratio of 0.35–0.36 and a fly ash content of 20%–30%. This mix proportion ensures key performance indicators such as strength, impermeability, and frost resistance, while also demonstrating good volume stability.

(2) Incorporating SF significantly enhances the mechanical strength and early-age ultimate tensile strain of concrete but increases mixture viscosity and autogenous shrinkage. Both NCC and the ACM improve crack resistance while effectively reducing the drying shrinkage of concrete. Although MgO expansive agent can induce early-age micro-expansion, its crack resistance index shows potential degradation at later ages, and it adversely affects the long-term frost resistance of concrete.

(3) EWM evaluation model allowed the quantification of the comprehensive crack resistance of concrete, resolving the inconsistencies found in traditional single-index methods. The derived CCRI identified SF, NCC, SF-FA, and MgO as the most effective admixtures. However, after accounting for fresh concrete workability constraints, NCC was determined to be the most balanced and effective solution for face slab concrete, ensuring the long-term safety and durability of rockfill dam concrete face slabs.

Disclosure statement

No potential conflict of interest was reported by the author(s).

Funding

This research was supported by the Deep Earth Probe and Mineral Resources Exploration-National Science and Technology Major Project (No. 2024ZD1000406), the National Natural Science Foundation of China (Grant No. 52509174) and the Yunnan Provincial S&T Program Project(Grant No. 202303AA080012).

Data availability statement

The data that support the findings of this study are available from the corresponding author upon reasonable request.

[1] Fang N, Zhou M, Zhang B, et al. A dual mortar finite element method for cross-corner contact problems and its application to concrete-faced rockfill dams. Computers and Geotechnics. 2025;185:107301.

[2] Li Y, Sun X, Li G, et al. Impact of concrete face cracks on the saturated and unsaturated seepage behavior of rockfill dams. Structures. 2024;61:105990.

[3] Vatani Oskouei A, Nazari R, Houshmand Khaneghahi M. Laboratory and in situ investigation of the compressive strength of CFRD concrete. Construction and Building Materials. 2020;242:118166.

[4] Li J, Lu X, Chen J, et al. Reliability-monitoring data coupled model for concrete slab safety evaluation of CFRD and its engineering application. Structures. 2022;35:520-530.

[5] Qu Y, Zou D, Chen K, et al. Three-dimensional refined analysis of seismic cracking and anti-seismic measures performance of concrete face slab in CFRDs. Computers and Geotechnics. 2021;139:104376.

[6] Liu Y, Zheng D, Cao E, et al. Cracking risk analysis of face slabs in concrete face rockfill dams during the operation period. Structures. 2022;40:621-632.

[7] Mao H, Xu N, Xiao P, et al. Microseismic characteristics and settlement analysis of concrete face rockfill dams on deep overburden layers during the filling process. Journal of Rock Mechanics and Geotechnical Engineering. 2025.

[8] Cen W, Wen L, Zhang Z, et al. Numerical simulation of seismic damage and cracking of concrete slabs of high concrete face rockfill dams. Water Science and Engineering. 2016;9(3):205-211.

[9] Wang Z, Liu S, Vallejo L, et al. Numerical analysis of the causes of face slab cracks in Gongboxia rockfill dam. Engineering Geology. 2014;181:224-232.

[10] Fu X, Zhao G, Wang M, et al. Comprehensive evaluation method for structural behavior of concrete dams in cold regions. Engineering Structures. 2023;278:115435.

[11] Chen B, He M, Huang Z, et al. Long-tern field test and numerical simulation of foamed polyurethane insulation on concrete dam in severely cold region. Construction and Building Materials. 2019;212:618-634.

[12] Li Z, Liu X, Sun Y, et al. Numerical simulation of frost heaving damage of earth-rock dam berms in cold regions with thermo-hydro-mechanical coupling. Cold Regions Science and Technology. 2024;223:104207.

[13] Zhang Y, Pan J, Sun X, et al. Simulation of thermal stress and control measures for rock-filled concrete dam in high-altitude and cold regions. Engineering Structures. 2021;230:111721.

[14] Zhu X, Zheng D, Zhang Y, et al. Study on the fracture paths and fracture surface characteristics of face slab concrete under variable temperature and wet-dry cycles. Construction and Building Materials. 2025;497:143965.

[15] Liu J, Tian Q, Wang Y, et al. Evaluation Method and Mitigation Strategies for Shrinkage Cracking of Modern Concrete. Engineering. 2021;7(3):348-357.

[16] Qin Z, Lai Y, Tian Y, et al. Frost-heaving mechanical model for concrete face slabs of earthen dams in cold regions. Cold Regions Science and Technology. 2019;161:91-98.

[17] Cao W, Liang N, Peng L, et al. Study the influence of basalt fiber on temperature cracks in mass concrete pile cap. Structures. 2025;80:109851.

[18] Liang N, Hu G, Zhou K, et al. Study on early-age cracking resistance of multi-scale polypropylene fiber reinforced concrete in restrained ring tests. Journal of Sustainable Cement-Based Materials. 2024;13(7):1050-1062.

[19] Wen C, Shen D, Luo Y, et al. Early-age autogenous shrinkage and tensile creep of concrete reinforced with polypropylene macro fiber. Journal of Sustainable Cement-Based Materials.

2023;12(10):1255-1269.
[20] Zhu T, Zhong W, Zhang D, et al. Steel fiber-driven enhancement in recycled concrete powder-GGBS geopolymer: A synergistic approach to mechanical strength, crack resistance, and microstructural refinement. Journal of Building Engineering. 2025;114:114399.
[21] Pan K, Ma C, Yu RC, et al. Multi-index evaluation of steel fiber's crack resistance enhancement in desert sand concrete under freeze-thaw cycles: Optimization, fracture, and mechanism. Construction and Building Materials. 2025;499:144059.
[22] Sagheb R, Miri M, Arab HG, et al. Cracking resistance and microstructure of green concretes made of waste crumb rubber and zeolite under full tensile-tearing fracture using ENDB specimen. Theoretical and Applied Fracture Mechanics. 2026;141:105303.
[23] Sagheb R, Miri M, Arab HG, et al. Toughness and energy based tensile-shear cracking resistance of green concrete developed using zeolite and waste rubber particles. Theoretical and Applied Fracture Mechanics. 2026;141:105263.
[24] Sanjaya BGV, Venkatesan S, Appuhamy JMRS, et al. Enhancing structural integrity and crack resistance of rubberized concrete using aqua-thermally treated rubber aggregates and recycled tire steel fibers for structural applications. Sustainable Materials and Technologies. 2025;46:e01720.
[25] Qu S, Pan C, Peng B, et al. Study on the crack resistance of concrete reinforced with flax fiber and multi-walled carbon nanotubes. Construction and Building Materials. 2025;488:141884.
[26] Algaifi HA, Baharom S, Syamsir A, et al. Experimental and finite element modeling of graphene tubes-reinforced rubberized Concrete: Enhancing flexural toughness and impact resistance. Journal of Building Engineering. 2025;111:113392.
[27] Fu H, Chai J, Xu Z, et al. Research on material selection and low-temperature anti-cracking mechanism of hydraulic asphalt concrete panels in the alpine region. Construction and Building Materials. 2024;423:135830.
[28] Wang L, Li G, Li X, et al. Influence of reactivity and dosage of MgO expansive agent on shrinkage and crack resistance of face slab concrete. Cement and Concrete Composites. 2022;126:104333.
[29] Guo J, Zhang S, Qi C, et al. Effect of calcium sulfoaluminate and MgO expansive agent on the mechanical strength and crack resistance of concrete. Construction and Building Materials. 2021;299:123833.
[30] Hu C, Lin X, Deng P, et al. Role of silica fume in autogenous shrinkage in MgO-K2HPO4-SiO2 cement system: Dual effects of chemical activation and pore structure refinement. Journal of Building Engineering. 2026;118:114987.
[31] Zhao J, Huang J, Wang Z, et al. Enhancing mechanical strength and reducing drying shrinkage in high-volume fly ash mortar: Synergistic effects of steel fibers and nano-SiO2. Journal of Materials Research and Technology. 2025;36:7351-7360.
[32] Shen D, Liu C, Wen C, et al. Restrained cracking failure behavior of concrete containing MgO compound expansive agent under adiabatic condition at early age. Cement and Concrete Composites. 2023;135:104825.
[33] Ji X, Wang B, Liu M, et al. Expansion and creep of concrete with expansive agents at variable temperature. Journal of Building Engineering. 2024;87:108982.
[34] Guo X, Liao L, Xie K, et al. Early-age mechanical and shrinkage performance of CaO-MgO expansive agent self-compacting concrete. Journal of Building Engineering. 2025;111:113165.
[35] Yang Y, Cheng Z, Zhang J, et al. C-S-H seeds prepared by wet milling of solid waste under fly ash dispersion: Enhancing the hydration and microstructure of OPC. Construction and Building Materials. 2025;493:143248.
[36] Hoe Woon T, Cheng Yong H, Yun Ming L, et al. Elucidating the interplay between pore microstructure and heavy metal leaching of rubber sludge in fly ash geopolymers. Journal of Environmental Chemical Engineering. 2025;13(5):117698.
[37] Zhang Y, Zhang X, Lu Z, et al. New insight into the effects of silane-modified silica fume on the performance of cement pastes. Cement and Concrete Research. 2025;190:107818.
[38] Bai Y-h, Lu Y, Zhang D-y. Preparation of nano-carbon black and silica fume modified foam concrete: Compressive strength, pore structure and electromagnetic property. Construction and Building Materials. 2023;369:130553.
[39] Sharma A, Garia S, Kale RC. Performance of self compacting concrete modified with wollastonite fibre and silica fume. Construction and Building Materials. 2025;497:143932.
[40] Sun J, Wang W, Liu C, et al. Nonlinear response of silica fume-steel slag-cement composites: A quartic polynomial modeling of hydration kinetics, pore refinement, and mechanical enhancement. Construction and Building Materials. 2025;494:143145..
[41] Li Z, Gong Y, Gao Y, et al. Mode III delamination characterization for composite laminates: an improved size-independent data reduction method for edge ring crack torsion test. Composites Science and Technology. 2025;271:111346.
[42] Gao B, Luo M, Lin K, et al. Fatigue crack growth and slow crack growth of HDPE pipes under internal pressure and flat plate compression. International Journal of Pressure Vessels and Piping. 2024;208:105155.
[43] Fang B, Qian Z, Song Y, et al. Evaluation of early crack resistance performance of concrete mixed with ternary minerals using temperature stress testing machine (TSTM). Journal of Cleaner Production. 2024;465:142780.
[44] Han Y, Zhou M, Wang Q, et al. Study on the fracture performance and crack resistance mechanism of microfilament steel fiber reinforced spontaneous combustion coal gangue aggregate concrete. Construction and Building Materials. 2025;473:141033.
[45] Ding J, Wang X, Sun Z, et al. Research on the cracking risk index of massive concrete based on Chemo-Thermo-Hygro-Mechanical multi-field coupling model. Journal of Building Engineering. 2024;98:111190.
[46] S. Liu, K. Fang, L. Zeng, et al., Review of concrete crack resistance evaluation index, Concrete. (5) (2004) 32-33. (in Chinese)
[47] G. Li, Evaluation of crack resistance of concrete, Adv. Sci. Technol. Water Resour. 21 (2) (2001) 33-36. (in Chinese)
[48] G. Huang, Discussion on crack resistance of hydraulic concrete, Water Power. (07) (2007) 90-93. (in Chinese)